Supplement of Earth Syst. Sci. Data, 17, 3009–3046, 2025
https://doi.org/10.5194/essd-17-3009-2025-supplement

Supplement of

CEDAR-GPP: spatiotemporally upscaled estimates of gross primary productivity incorporating CO_2 fertilization

Yanghui Kang et al.

Correspondence to: Yanghui Kang (yanghuikang@vt.edu) and Trevor F. Keenan (trevorkeenan@berkeley.edu)

This PDF file includes:

Sections S1 to S2

Table S1 to S2

Figure S1 to S20

SI References

S1. C3/C4 Classification in Eddy Covariance Sites

We classified eddy covariance sites as C3 or C4 based on species information from site metadata and relevant peer-reviewed articles. For sites where such information was unavailable, we referred to a C4 plant percentage map (Still et al., 2009). When constructing datasets for model training, we removed sites dominated as C4 plant and retained sites with a mixed C3 and C4 vegetation, as well as agricultural sites with crop rotations involving C3 and C4 plants. Below we provide a list of sites dominated by C3 plants, C4 plants, a mixture of C3/C4 plants, and C3/C4 crop rotations.

<u>Sites dominated by C3 plants</u>

AR-SLu, AR-Vir, AT-Neu, AU-Ade, AU-ASM, AU-Cpr, AU-Cum, AU-DaP, AU-DaS, AU-Dry, AU-Fog, AU-Gin, AU-GWW, AU-How, AU-Lox, AU-RDF, AU-Rig, AU-Rob, AU-Tum, AU-Wac, AU-Whr, AU-Wom, BE-Bra, BE-Dor, BE-Lcr, BE-Maa, BE-Vie, BR-Sa1, BR-Sa3, CA-Ca1, CA-Ca2, CA-Ca3, CA-Cbo, CA-Gro, CA-Man, CA-NS1, CA-NS2, CA-NS3, CA-NS4, CA-NS5, CA-NS6, CA-NS7, CA-Oas, CA-Obs, CA-Qc2, CA-Qfo, CA-SF1, CA-SF2, CA-SF3, CA-SJ2, CA-TP1, CA-TP2, CA-TP3, CA-TP4, CA-TPD, CA-WP1, CA-WP2, CA-WP3, CG-Tch, CH-Aws, CH-Cha, CH-Dav, CH-Fru, CH-Lae, CH-Oe1, CH-Oe2, CN-Cha, CN-Cng, CN-Dan, CN-Din, CN-Du2, CN-Du3, CN-Ha2, CN-HaM, CN-Qia, CZ-BK1, CZ-BK2, CZ-Lnz, CZ-RAJ, CZ-Stn, CZ-wet, DE-Akm, DE-Geb, DE-Gri, DE-Hai, DE-HoH, DE-Hte, DE-Hzd, DE-Kli, DE-Lkb, DE-Lnf, DE-Obe, DE-RuR, DE-RuS, DE-RuW, DE-Seh, DE-SfN, DE-Spw, DE-Tha, DE-Zrk, DK-Eng, DK-Fou, DK-Gds, DK-Sor, ES-Abr, ES-Agu, ES-Amo, ES-Cnd, ES-LgS, ES-LJu, ES-LM1, ES-LM2, ES-Ln2, FI-Hyy, FI-Jok, FI-Ken, FI-Let, FI-Lom, FI-Qvd, FI-Sii, FI-Sod, FI-Var, FR-Aur, FR-Bil, FR-FBn, FR-Fon, FR-Hes, FR-LBr, FR-LGt, FR-Pue, GF-Guy, GH-Ank, GL-Dsk, GL-NuF, GL-ZaF, GL-ZaH, IE-Cra, IL-Yat, IT-BFt, IT-CA1, IT-CA2, IT-CA3, IT-Col, IT-Cp2, IT-Cpz, IT-Isp, IT-La2, IT-Lav, IT-Lsn, IT-MBo, IT-Noe, IT-PT1, IT-Ren, IT-Ro1, IT-Ro2, IT-SR2, IT-SRo, IT-Tor, JP-MBF, JP-SMF, MY-PSO, NL-Hor, NL-Loo, PA-SPn, RU-Che, RU-Cok, RU-Fy2, RU-Fyo, RU-Ha1, SD-Dem, SE-Deg, SE-Htm, SE-Lnn, SE-Nor, SE-Ros, SE-Svb, SJ-Adv, SJ-Blv, SN-Dhr, US-Atq, US-Bar, US-Bi1, US-Blo, US-CRT, US-Dk1, US-Dk2, US-Dk3, US-Fmf, US-FR2, US-Fuf, US-GBT, US-GLE, US-Ha1, US-Ho1, US-Ivo, US-KS1, US-KS2, US-Lin, US-Los, US-Me1, US-Me2, US-Me3, US-Me4, US-Me5, US-Me6, US-Men, US-MMS, US-Mpj, US-Myb, US-NR1, US-Oho, US-ORv, US-OWC, US-PFa, US-Pnp, US-Prr, US-Rls, US-Rms, US-Rws, US-Ses, US-SRC, US-SRM, US-Sta, US-Syv, US-Ton, US-Tw1, US-Tw3, US-Tw4, US-Twt, US-Uaf, US-UMB, US-UMd, US-Var, US-Vcm, US-Vcp, US-WCr, US-Wgr, US-Whs, US-Wi0, US-Wi1, US-Wi2, US-Wi3, US-Wi4, US-Wi5, US-Wi6, US-Wi7, US-Wi8, US-Wi9, US-Wjs, US-WPT, ZM-Mon

<u>Sites dominated by C4 plants</u>

AU-Stp, AU-TTE, IT-BCi, PA-SPs, US-AR1, US-AR2, US-ARb, US-ARc, US-Bi2, US-IB2, US-LWW, US-Ne1, US-Ro4, US-SRG, US-Tw2, US-Wkg

<u>Sites with a mixture of C3 and C4 plants</u>

AU-Emr, AU-Ync, CN-Sw2, FR-EM2, US-ARM, US-Cop, US-KFS, US-Seg

<u>Sites with rotations of C3 and C4 crops</u>

BE-Lon, FR-Gri, FR-Lam, US-Ne2, US-Ne3, US-Ro1, US-Ro5, US-Ro6

S2. Note on XGBoost Hyperparameters

During the nested cross-validation (Main text Section 2.3.3), XGBoost model hyperparameters were determined using a randomized search based on 3-fold cross-validation within each training set. This process generated a best-fit parameter set for each of the five folds. When generating the global product, the final hyperparameters were determined based on a majority vote from the five best-fit parameter sets. For the short-term model setups, the XGBoost models were trained with 500 estimators (parameter "n_estimator" in the XGBoost python API), a learning rate ("learning_rate" of 0.01, and a subsample ratio of columns/features ("colsample_bytree") of 0.3 for each tree. For the long-term model setups, the XGBoost models used 300 estimators, a learning rate of 0.05, and a subsample ratio of columns of 0.3. Note that adding the CO_2 features to the models or using NT versus DT GPP did not change the selected best-fit parameter sets.

Table S1. List of predictors used in different temporal model setup

Name	Source/Dataset	Unit	Used in Short-term	Used in Long-term
Air temperature	ERA5-Land	K	✓	✓
Skin temperature		K	✓	✓
Precipitation		m	✓	✓
Precipitation 3-month lag		m	✓	✓
VPD		kPa	✓	✓
Potential ET		m	✓	✓
Surface downwelling solar radiation		J/m2		✓
Surface reflectance Band 1 (red)	MCD43C4	-	✓	
Surface reflectance Band 2 (nir)		-	✓	
Surface reflectance Band 3 (blue)		-	✓	
Surface reflectance Band 4 (green)		-	✓	
Surface reflectance Band 5 (SWIR1)		-	✓	
Surface reflectance Band 6 (SWIR2)		-	✓	
Surface reflectance Band 7 (SWIR3)		-	✓	
Normalized Difference Vegetation,Index (NDVI)		-	✓	
kNDVI [a]		-	✓	
Enhanced Vegetation Index (EVI)		-	✓	
Normalized Difference Water Index,(NDWI) [b]		-	✓	
CI_{Green} [c]		-	✓	
NIRv [d]		-	✓	
Percentage of snow cover		%	✓	
fPAR	MCD15A3H (after 2002/07); MOD15A2H (before 2002/07)	-	✓	
LAI		-	✓	
NDVI	GIMMS NDVI4g	-		✓
LAI	GIMMS LAI4g	-		✓
Daytime land surface temperature	MYD11A1 (after 2002/07); MOD11A1 (before 2002/07)	K	✓	
Nighttime land surface temperature		K	✓	

All-sky daily average SIF	CSIF	$mW\ m^{-2}nm^{-1}sr^{-1}$	✓	
Photosynthetic Active Radiation (PAR)	BESS PAR	W/m^2	✓	
Diffuse PAR		W/m^2	✓	
Shortwave downwelling radiation		W/m^2	✓	
Soil moisture	ESACCI Soil Moisture	%	✓	
Plant Function Type (one-hot encoding)	MCD12Q1	-	✓	✓
Climate zone (one-hot encoding)	Koppen-Geiger	-	✓	✓
C4 vegetation percentage	ISLSCP II C4 Vegetation Percentage	%	✓ (only in ST_CFE-ML and ST_CFE-Hybrid setups)	✓ (only in LT_CFE-Hybrid setup)
Atmospheric CO_2 concentration	ESLR	ppm	✓ (only in CFE-ML and CFE-Hybrid setups)	✓ (only in LT_CFE-Hybrid setup)

a. kNDVI (Camps-Valls et al., 2021)

b. NDWI (Gao, 1996)

c. CIgreen (Gitelson, 2005)

d. NIRv (Badgley et al., 2017)

Table S2. Cross-validation performance of ten CEDAR-GPP model setups

Model Setup	Monthly			MSC			Monthly anomalies			Cross-site		
	RMSE	Bias	r2	RMSE	Bias	r2	RMSE	Bias	r2	RMSE	Bias	r2
ST_Baseline_NT	2.04	-0.08	0.72	1.65	0.01	0.77	1.23	0.00	0.10	1.15	0.02	0.63
ST_CFE-ML_NT	2.05	-0.08	0.72	1.65	0.01	0.77	1.23	0.00	0.11	1.16	0.02	0.63
ST_CFE-Hybrid_NT	2.04	-0.08	0.72	1.64	0.00	0.77	1.23	0.00	0.11	1.15	0.01	0.64
LT_Baseline_NT	2.23	-0.05	0.66	1.85	0.06	0.71	1.26	0.00	0.06	1.29	0.07	0.54
LT_CFE-Hybrid_NT	2.22	-0.07	0.67	1.84	0.04	0.72	1.26	0.00	0.06	1.28	0.05	0.55
ST_Baseline_DT	1.95	-0.07	0.71	1.55	0.01	0.78	1.20	0.00	0.10	1.06	0.02	0.66
ST_CFE-ML_DT	1.95	-0.05	0.72	1.55	0.03	0.78	1.21	0.00	0.10	1.05	0.04	0.67
ST_CFE-Hybrid_DT	1.94	-0.08	0.72	1.54	0.00	0.78	1.20	0.00	0.10	1.04	0.00	0.67
LT_Baseline_DT	2.11	-0.04	0.67	1.73	0.06	0.73	1.24	0.00	0.05	1.17	0.06	0.59
LT_CFE-Hybrid_DT	2.10	-0.02	0.67	1.72	0.08	0.73	1.24	0.00	0.05	1.16	0.09	0.59

Table S3. Sites from the OzFlux FluxNet dataset used for independent validation.

Site ID	IGBP	Koppen zone	Data range	No. of site-months
AU-ASM	SAV	Arid	2010-2019	111
AU-Adr	SAV	Tropical	2007-2009	19
AU-Boy	SAV	Temperate	2017-2019	24
AU-Cpr	SAV	Arid	2011-2019	104
AU-Cum	EBF	Temperate	2014-2019	71
AU-Dry	WSA	Tropical	2010-2019	90
AU-GWW	SAV	Arid	2013-2019	83
AU-Lit	SAV	Tropical	2015-2019	53
AU-Rgf	CRO	Temperate	2016-2019	39
AU-Stp	GRA	Arid	2009-2019	114
AU-War	EBF	Temperate	2013-2019	53

Table S4. CEDAR-GPP model performance based on independent data from the OzFlux FluxNet dataset

Model Setup	**R^2**				**RMSE**			
	Overall	MSC	Anomalies	Cross-site	Overall	MSC	Anomalies	Cross-site
ST_Baseline_NT	0.75	0.77	0.33	0.77	1.27	1.23	0.77	1.00
ST_CFE-Hybrid_NT	0.75	0.77	0.33	0.77	1.27	1.23	0.77	0.99
ST_CFE-ML_NT	0.75	0.77	0.33	0.76	1.27	1.24	0.77	1.01
LT_Baseline_NT	0.74	0.80	0.26	0.77	1.29	1.15	0.81	0.98
LT_CFE-Hybrid_NT	0.74	0.79	0.26	0.76	1.28	1.16	0.81	1.00
ST_Baseline_DT	0.73	0.74	0.50	0.69	1.40	1.40	0.67	1.17
ST_CFE-Hybrid_DT	0.73	0.74	0.50	0.69	1.39	1.40	0.67	1.16
ST_CFE-ML_DT	0.74	0.74	0.50	0.69	1.38	1.39	0.67	1.16
LT_Baseline_DT	0.74	0.78	0.43	0.72	1.37	1.29	0.71	1.11
LT_CFE-Hybrid_DT	0.74	0.77	0.43	0.71	1.38	1.30	0.71	1.13

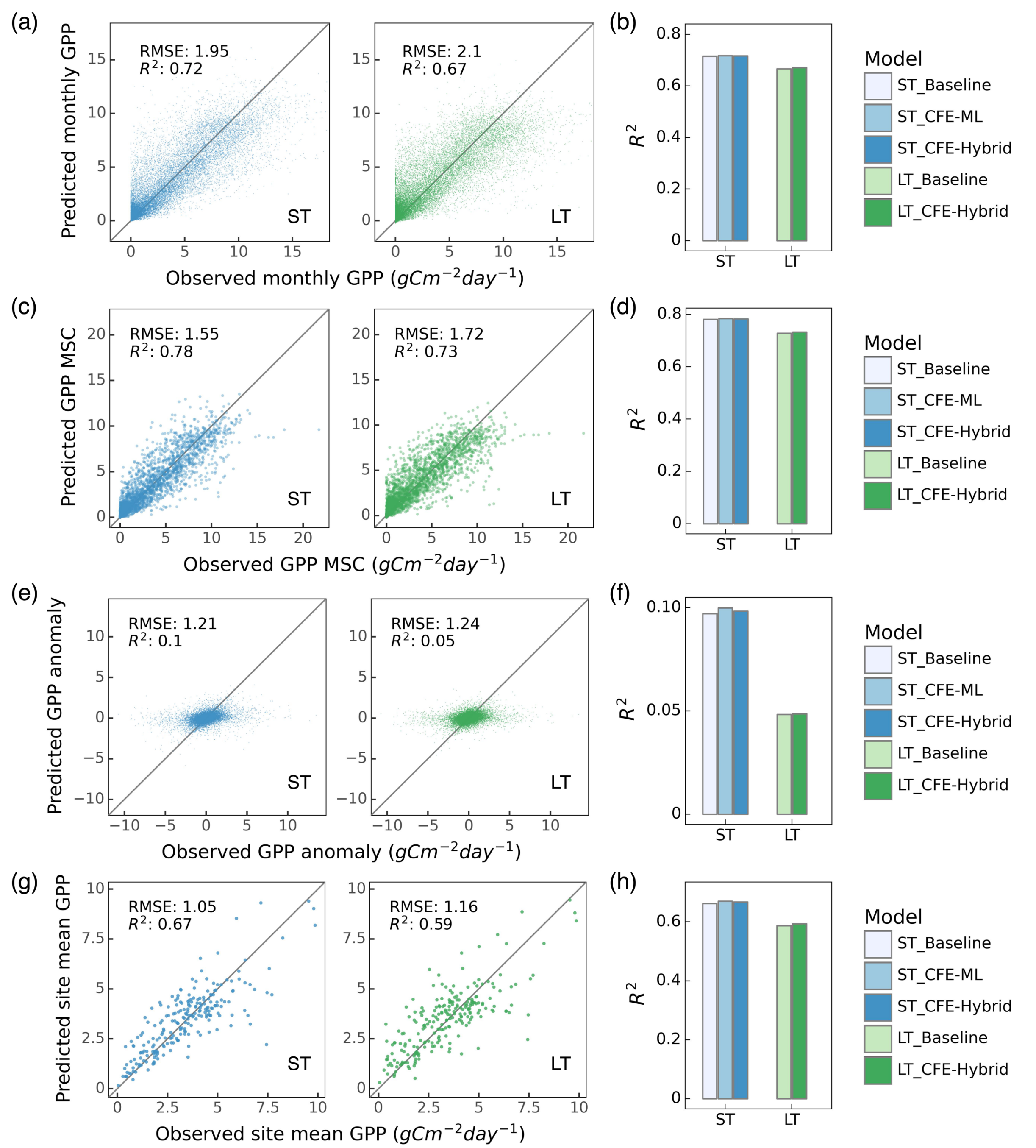

Figure S1. Machine learning model performance in predicting monthly GPP and its spatial and temporal variability (DT models only). Scatter plots illustrated relationships between model predictions and observations for monthly GPP (a), mean seasonal cycles (MSC) (c), monthly anomaly (e), and cross-site variability (g) for ST_CFE-Hybrid_NT (left, blue) and LT_CFE-Hybrid_NT (right, green) models. Corresponding bar plots show the R2 values for five all ten NT model setups in predicting monthly GPP (b), MSC (d), monthly anomaly (f), and cross-site variability (h).

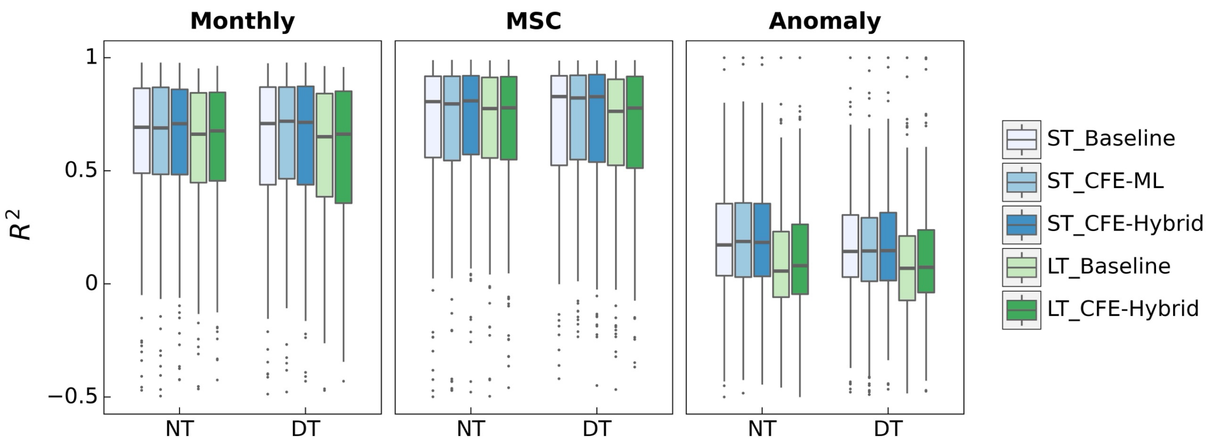

Figure S2. Site-level performance of ten CEDAR-GPP model setups in predicting monthly GPP, GPP mean seasonal cycle, and monthly anomalies. The distribution of model accuracy (R^2) across sites is summarized by the boxplots. Each box represents the interquartile range (IQR), the line inside the box indicates the median, and the whiskers extend to the smallest and largest values within 1.5 times the IQR. Points outside this range are plotted as outliers.

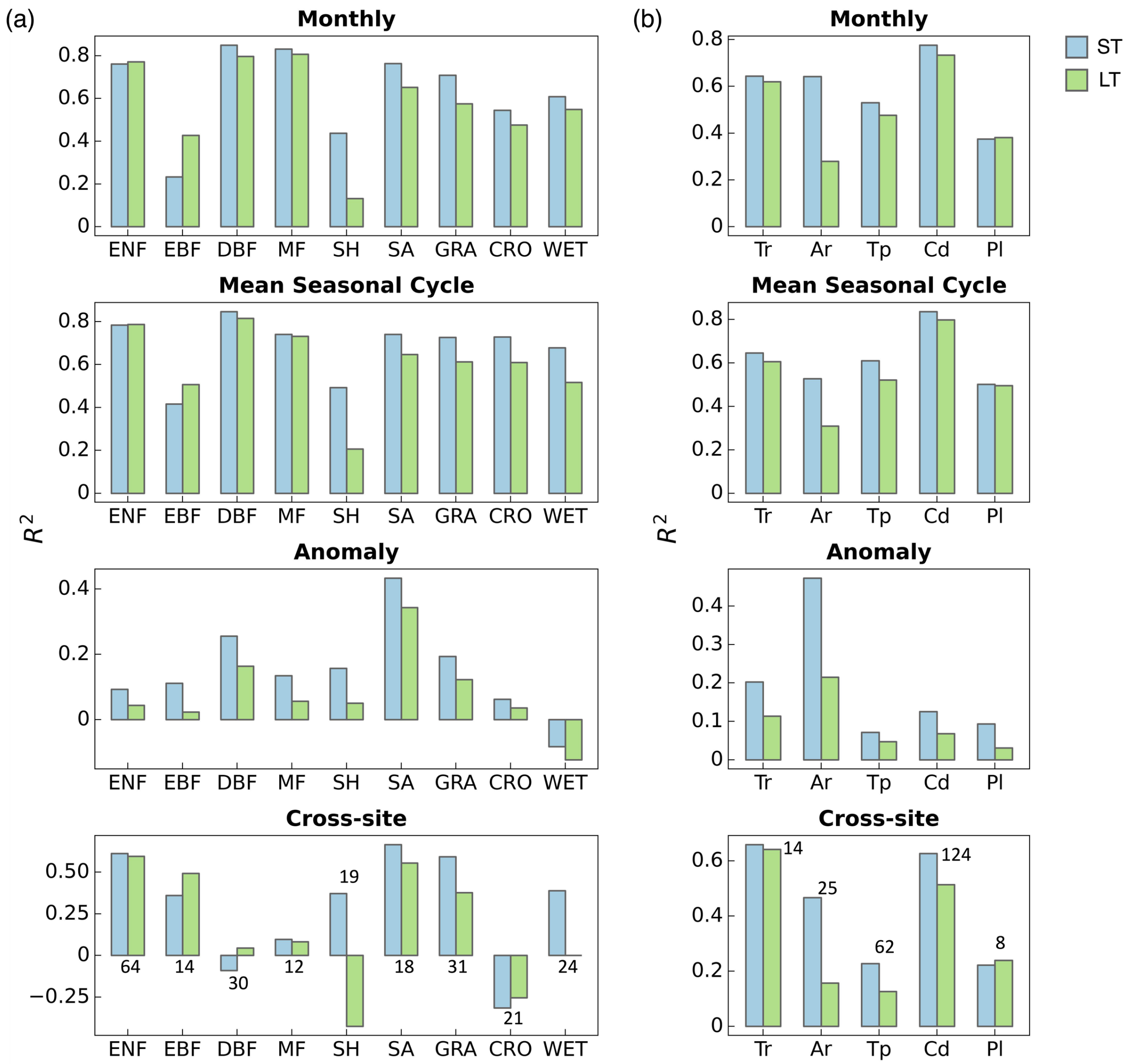

Figure S3. Performance (R^2) of the ST_CFE-Hybrid_DT (blue) and LT_CFE-Hybrid_DT (green) models on GPP spatiotemporal estimation by plant functional types (a) and climate zones (b). The cross-site panels included the number of sites within each category. ENF: evergreen needleleaf forest, EBF: evergreen broadleaf forest, DBF: deciduous broadleaf forest, MF: mixed forest, SH: shrubland, SA: savanna, GRA: grassland, CRO: cropland, WET: wetland. Tr: tropical, Ar: arid, Tp: temperate, Cd: cold, Pl: polar.

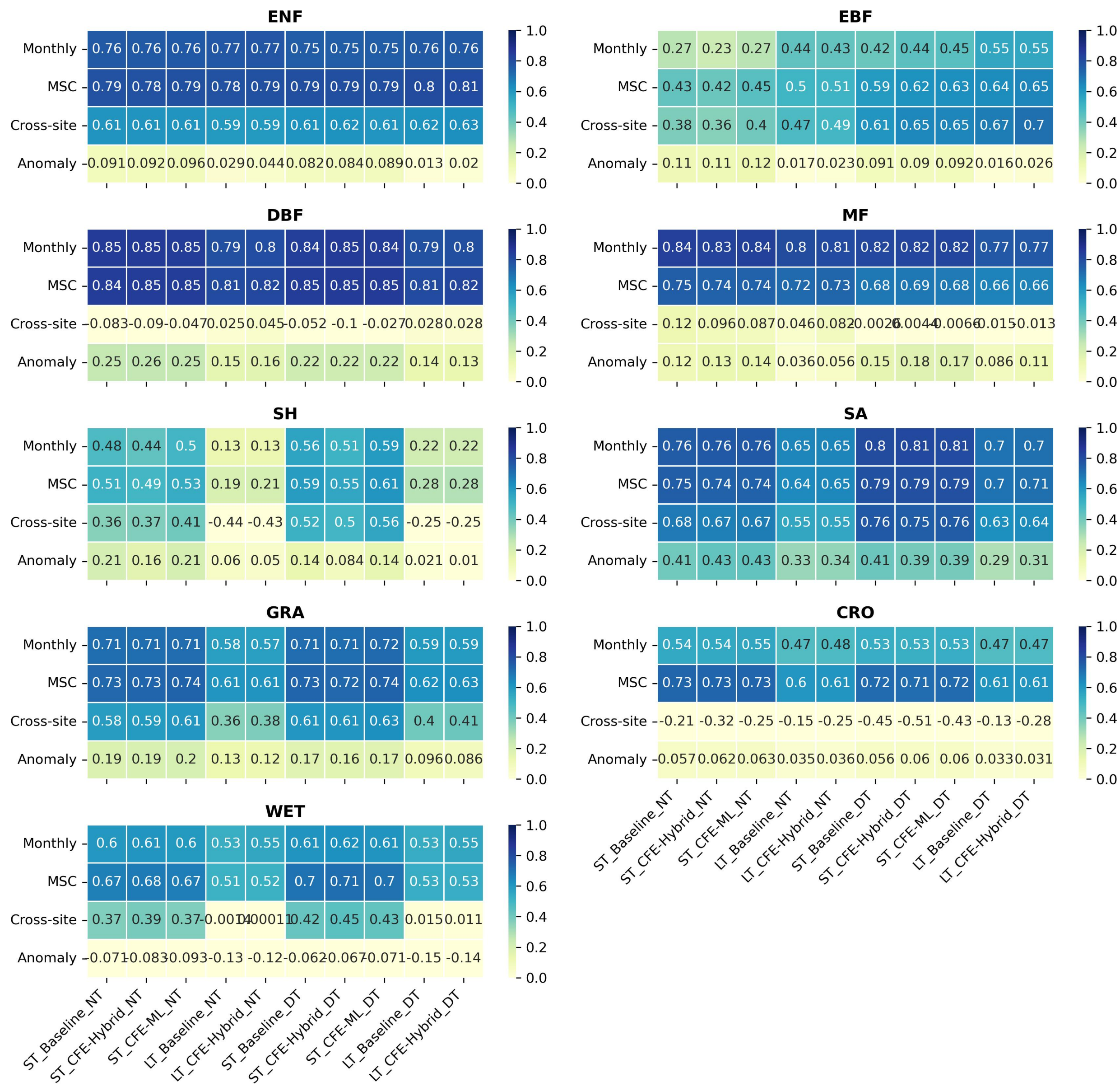

Figure S4. Performance heatmap (R^2) of the ten CEDAR-GPP models on GPP spatiotemporal estimation by plant functional types.

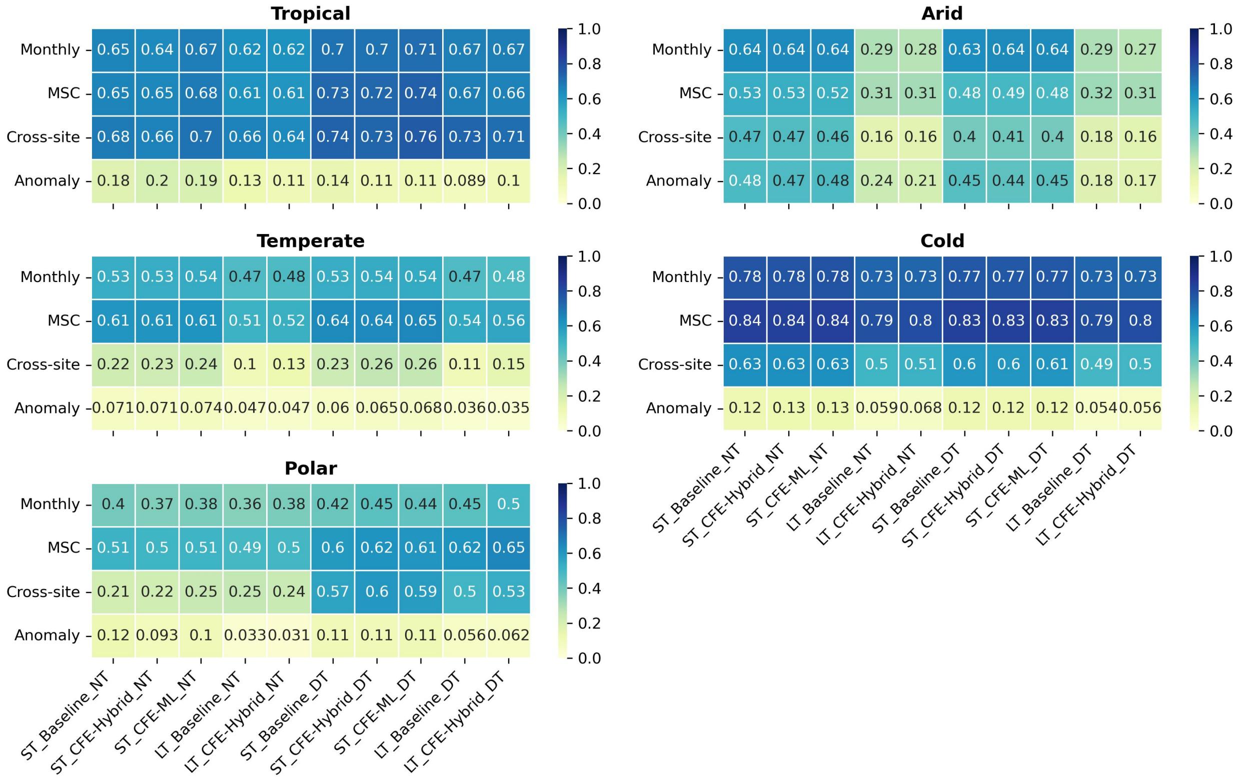

Figure S5. Performance heatmap (R^2) of the ten CEDAR-GPP models on GPP spatiotemporal estimation by Koppen climate zones.

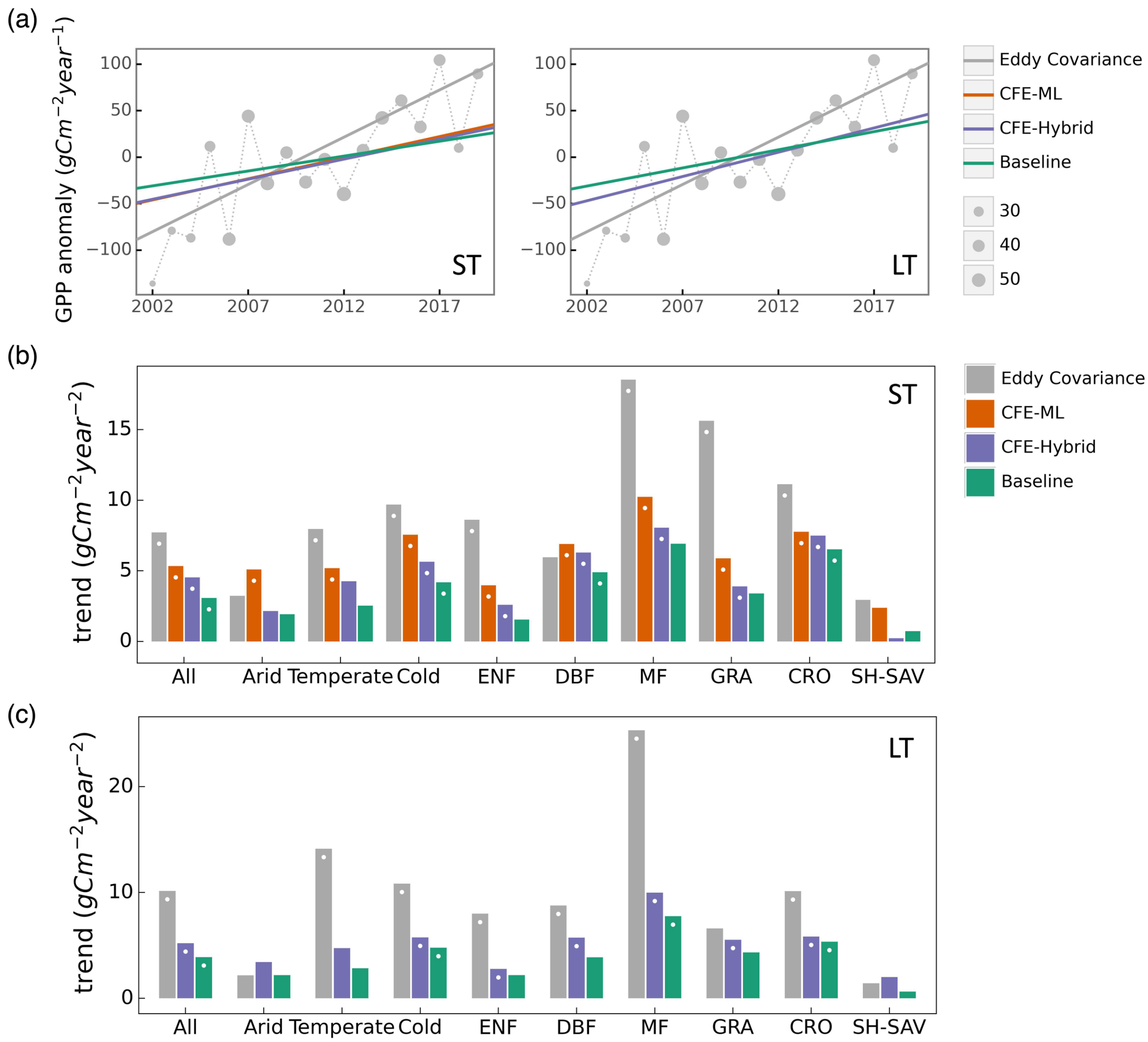

Figure S6. Comparison of observed and predicted GPP (from DT models only) trends across eddy covariance flux towers. (a) Aggregated annual GPP anomaly from 2002 to 2019 and trend lines from eddy covariance (EC) measurements, and three CFE model setups (short-term, night-time partitioning) for ST (left) and LT (right) models. The size of grey circle markers is proportional to the number of sites. (b) Annual trends from eddy covariance measurements and the short-term (ST) CEDAR-GPP model setups. (c) Annual trends from eddy covariance measurements and the long-term (LT) CEDAR-GPP model setups.

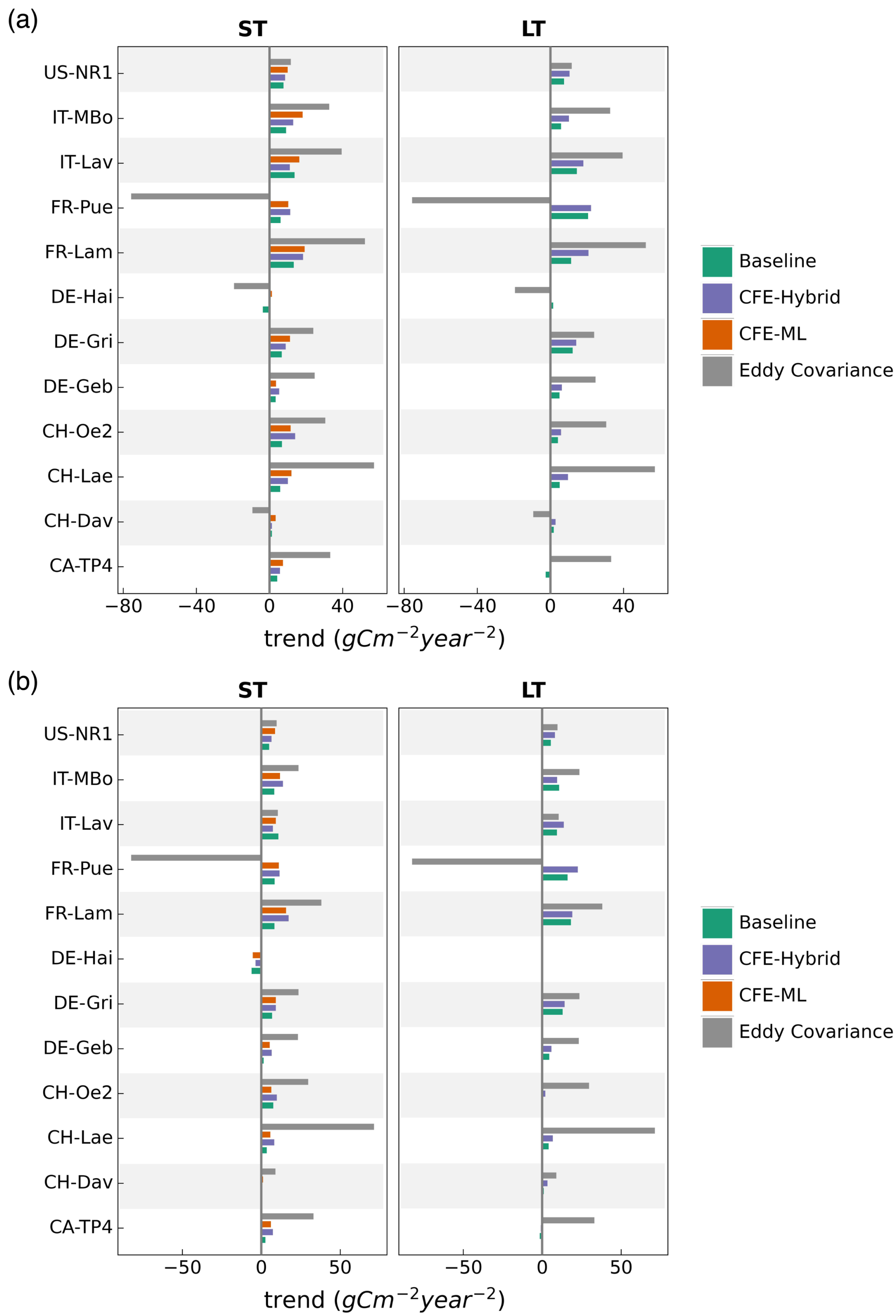

Figure S7. Comparison of observed and predicted GPP trends from (a) NT models and (b) DT models in long-term flux sites. Only sites with at least ten years of data and a significant annual trend (p-value < 0.3) are shown.

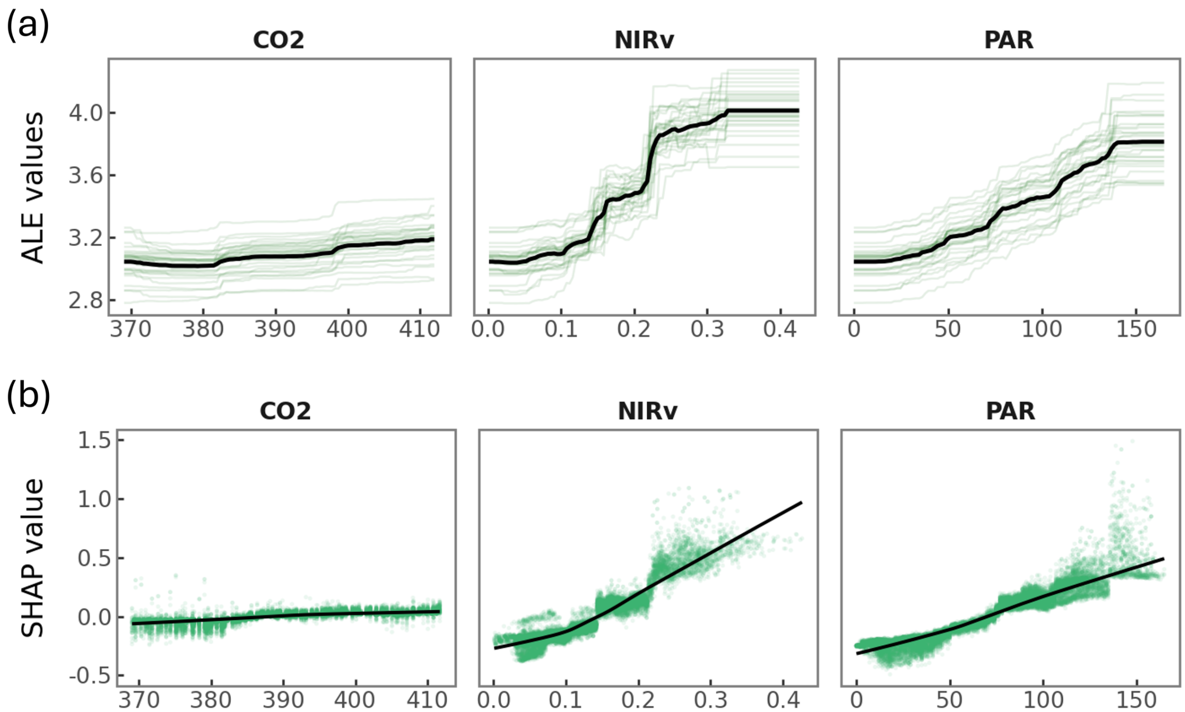

Figure S8. GPP responses to CO2, NIRv, and PAR from the ST_CFE-ML_NT model evaluated with (a) the Accumulated Local Effectis (ALE) and (b) the SHAP (SHapley Additive exPlanations) explaining approaches. Light green lines in (a) represent ALE response curves of 30 model ensembles, and the thick black presents the ensemble mean curve. Green dots in (b) correspond to SHAP values of individual samples (i.e. GPP observation from one site-month). Black solid lines in (b) are LOESS (local regression) curves.

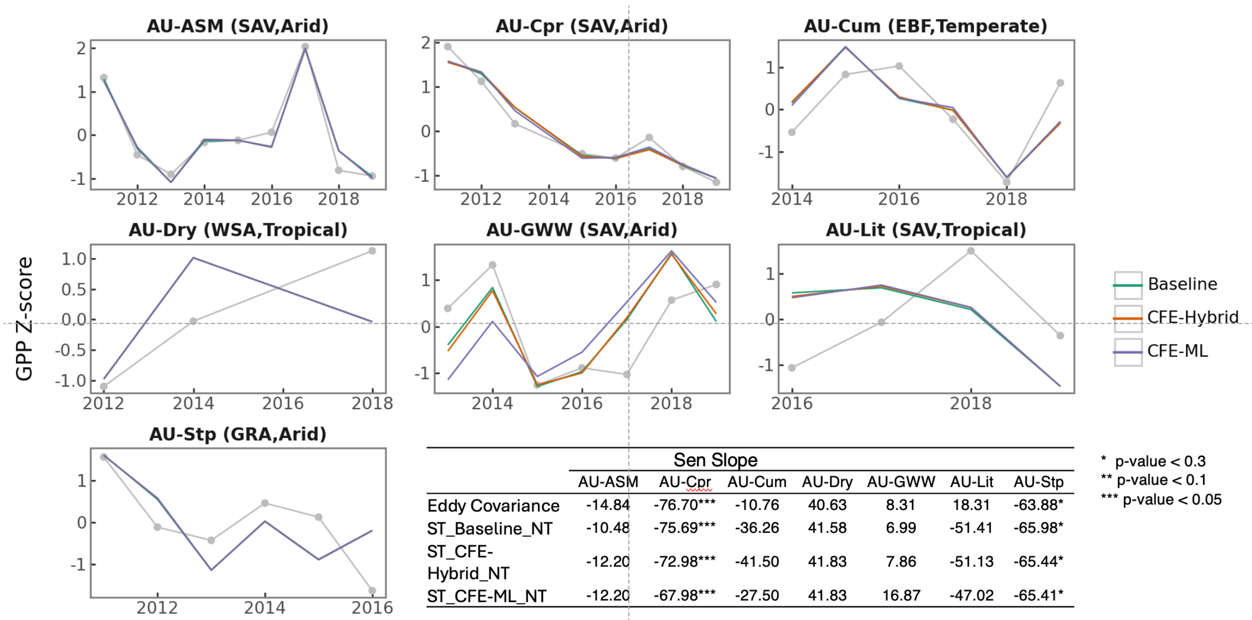

Sen Slope	AU-ASM	AU-Cpr	AU-Cum	AU-Dry	AU-GWW	AU-Lit	AU-Stp
Eddy Covariance	-14.84	-76.70***	-10.76	40.63	8.31	18.31	-63.88*
ST_Baseline_NT	-10.48	-75.69***	-36.26	41.58	6.99	-51.41	-65.98*
ST_CFE-Hybrid_NT	-12.20	-72.98***	-41.50	41.83	7.86	-51.13	-65.44*
ST_CFE-ML_NT	-12.20	-67.98***	-27.50	41.83	16.87	-47.02	-65.41*

Figure S9. Standardized annual GPP anomalies from eddy covariance data and estimated by CEDAR-GPP for seven independent (not included in model training and development) sites from the OzFlux FluxNet dataset. The results compare three CEDAR-GPP model setups – ST_Baseline_NT, ST_CFE-Hybrid_NT, and ST_CFE-ML_NT. Eddy covariance GPP was partitioned using the Night-time (NT) approach. The bottom right inset table lists the annual GPP trends based on Sen's slopes and the Mann-Kendall test.

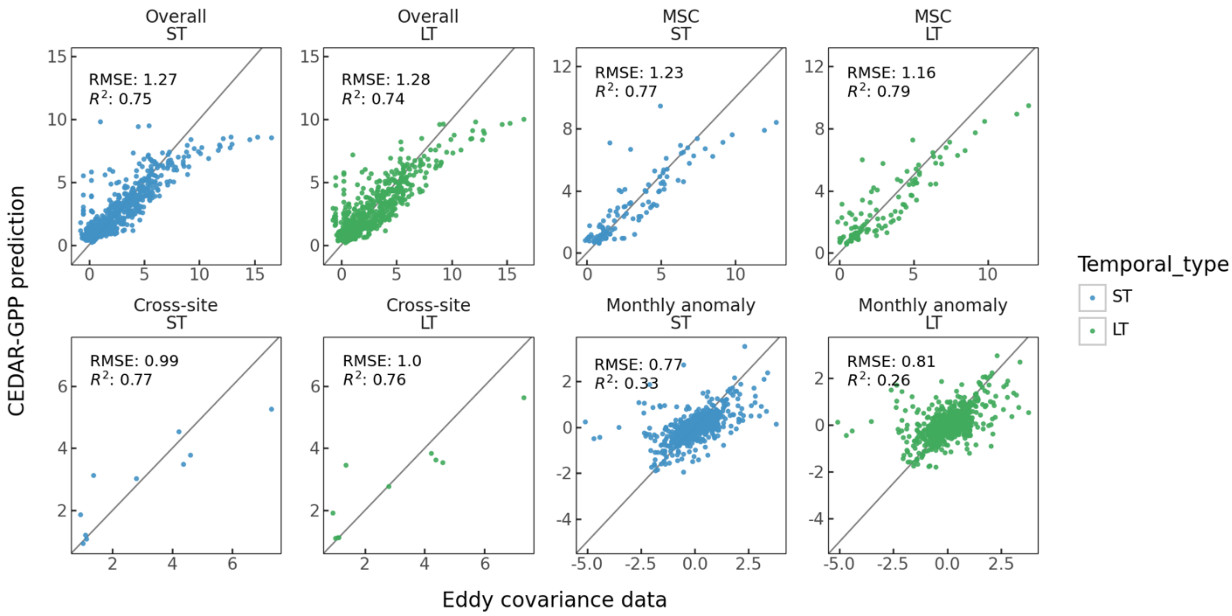

Figure S10. CEDAR-GPP performance in estimating monthly GPP, mean seasonal cycle, monthly anomalies, and spatial variations in 11 independent sites from the OzFlux FluxNet dataset, which was not included in model training and development.

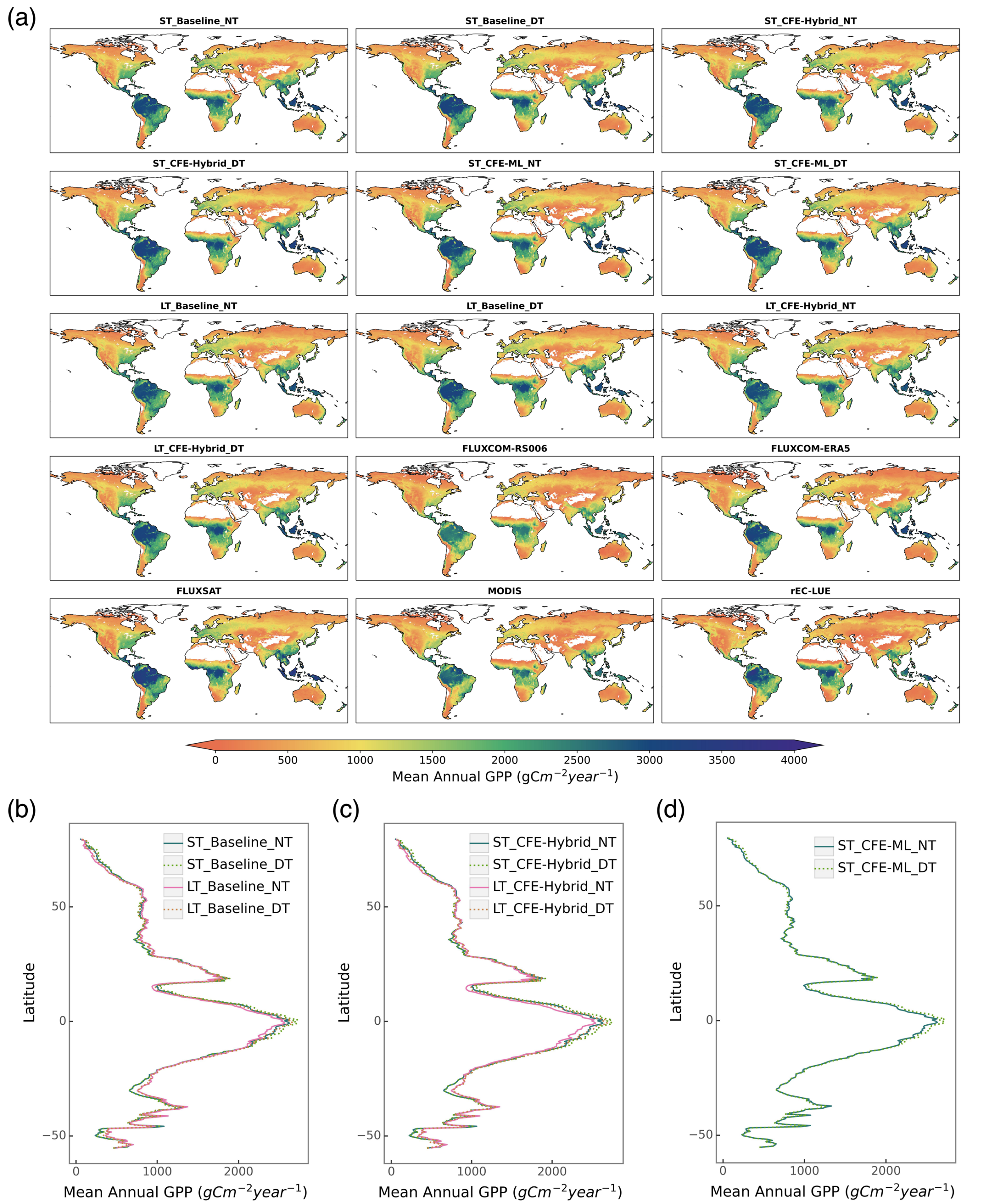

Figure S11. Global patterns of mean annual GPP from CEDAR-GPP product and other GPP datasets.

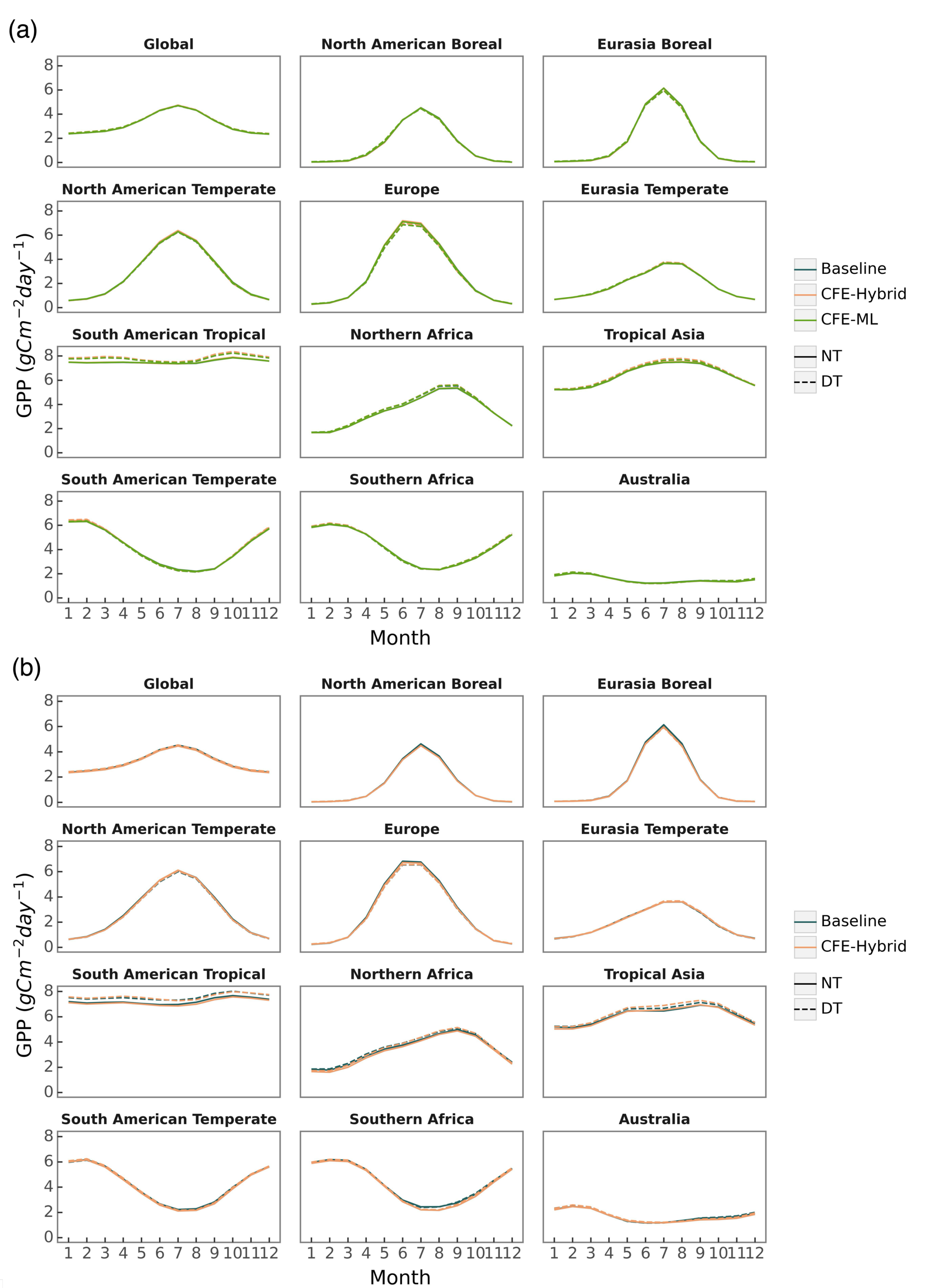

Figure S12. Global and regional mean seasonal cycles from CEDAR-GPP short-term (ST) (a) and long-term (LT) (b) datasets. Figure S18 shows a map of 11 TransCom regions.

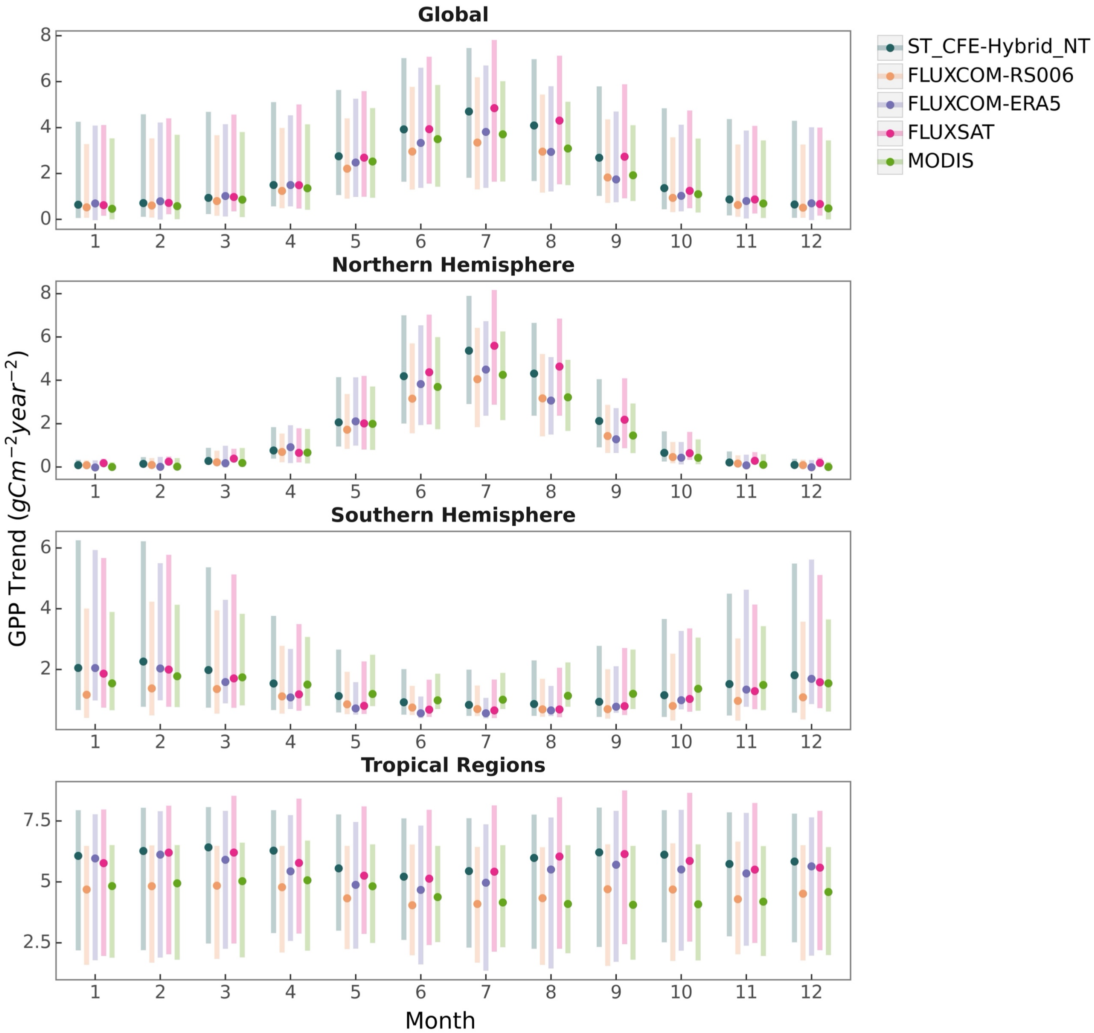

Figure S13. Comparison of GPP mean seasonal cycle between different datasets on a global scale, specifically within the Northern Hemisphere (20ºN - 90ºN), Southern Hemisphere (20ºS - 60ºS), and Tropical regions (20ºN - 20ºS). Monthly means were averaged from 2001 to 2018 for all datasets. Dots represent the spatial medians and vertical bars indicate the interquartile range (25th to 75th percentiles).

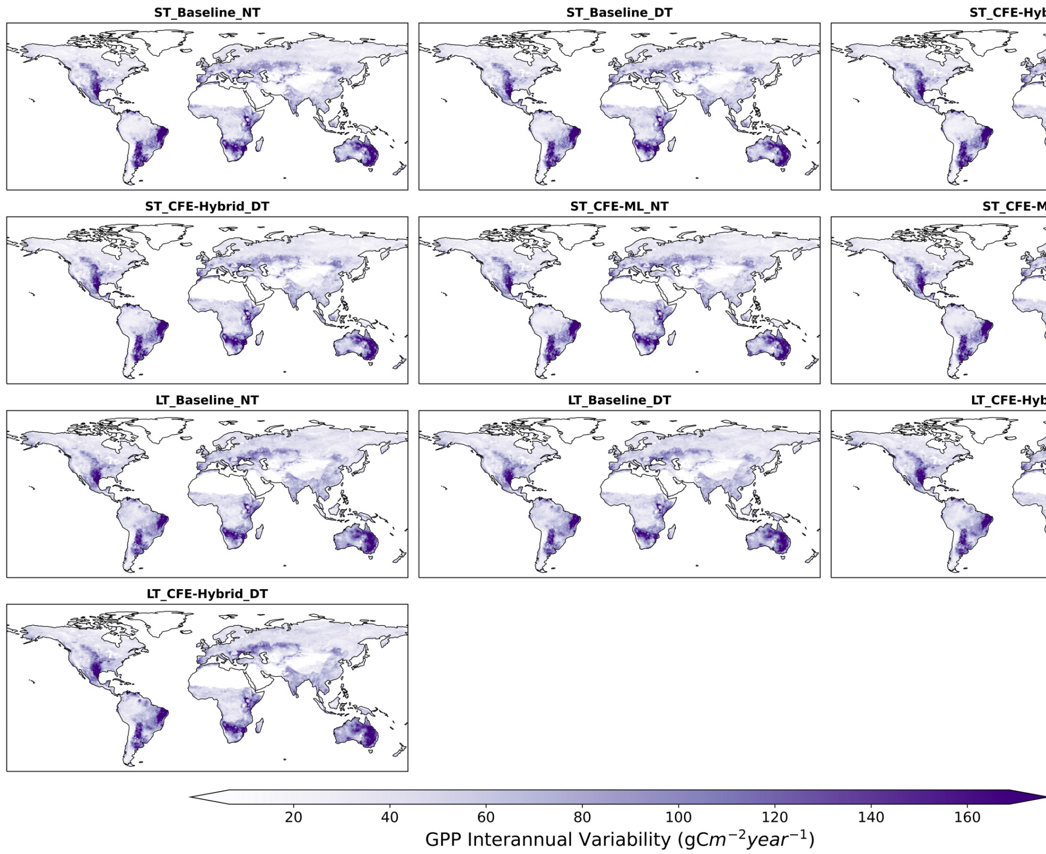

Figure S14. Spatial patterns of GPP interannual variability from ten CEDAR-GPP extracted from 2001 to 2018.

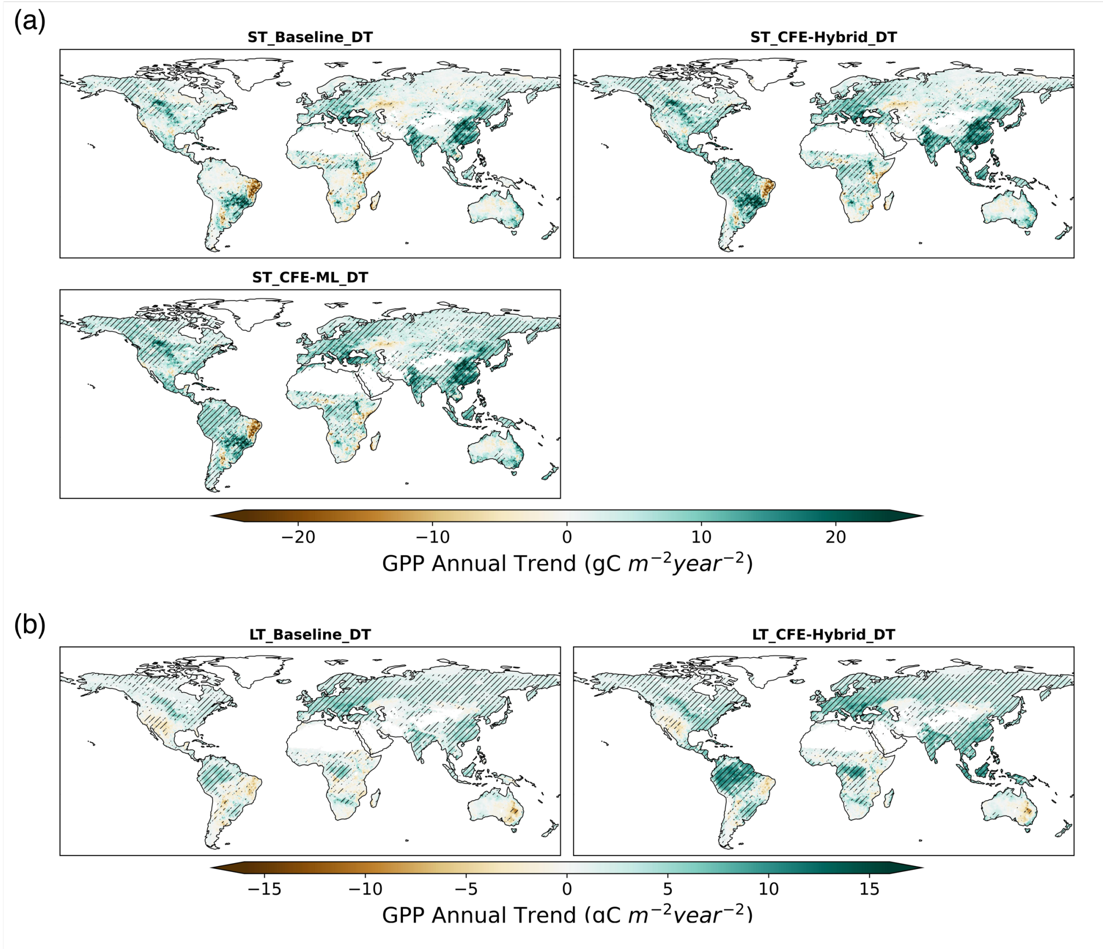

Figure S15. Annual GPP trends (a) over 2001 – 2018 from short-term day-time CEDAR GPP datasets and (b) over 1982 – 2018 for long-term day-time CEDAR-GPP datasets. Hatched areas indicate the GPP trend that is statistically significant at $p < 0.05$ level under the Mann-Kendal test.

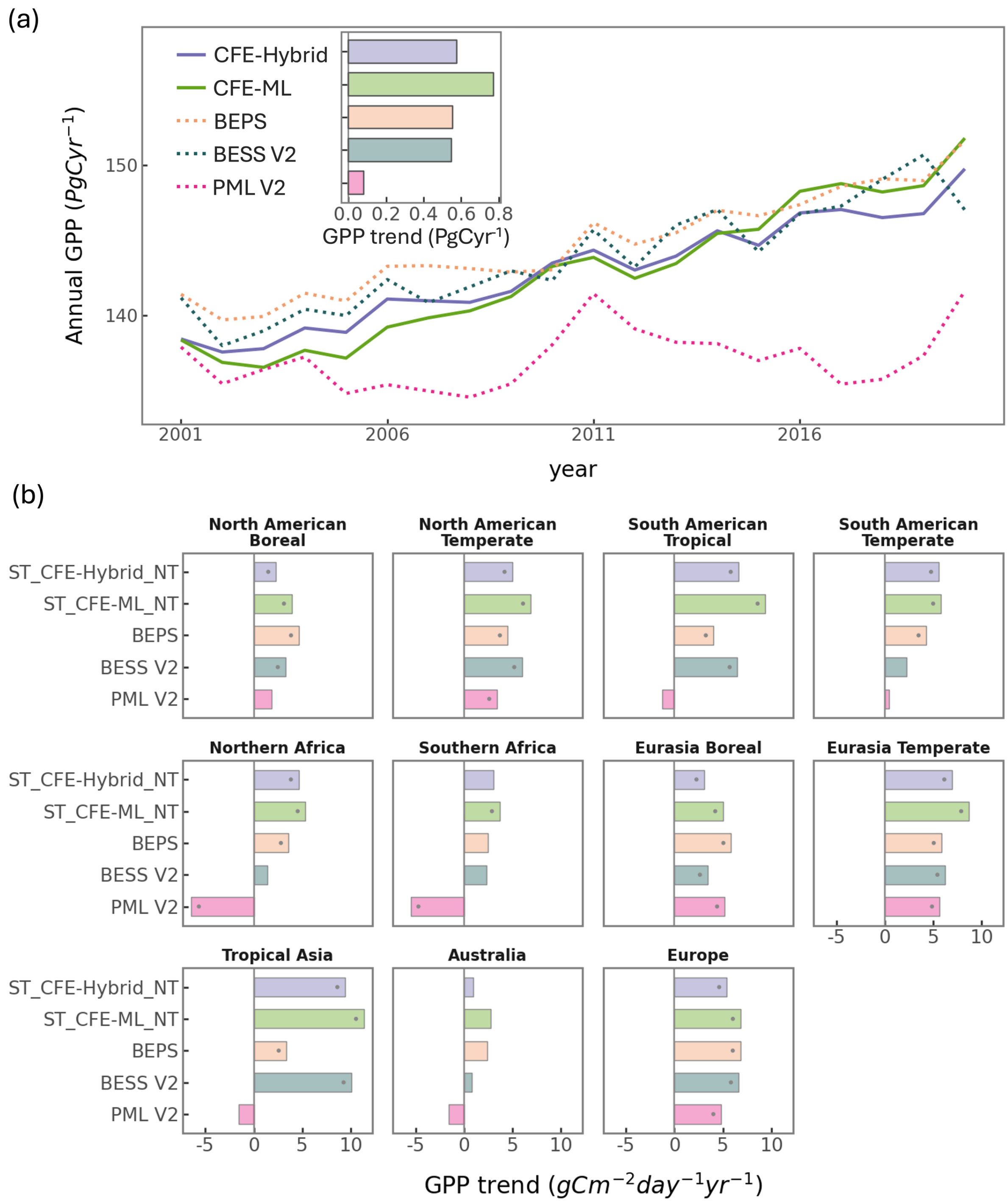

Figure S16. Global and regional GPP trends from 2001 to 2020 short-term night-time CEDAR GPP datasets, BEPS, BESS v2, and PML V2. a) Global annual GPP over time, with an inset showing GPP trends. b) GPP trend in 11 TransCom regions. Bars marked with a grey dot represent statistically significant trends at $p < 0.05$ level under the Mann-Kendal test. Figure S18 shows a map of 11 TransCom regions.

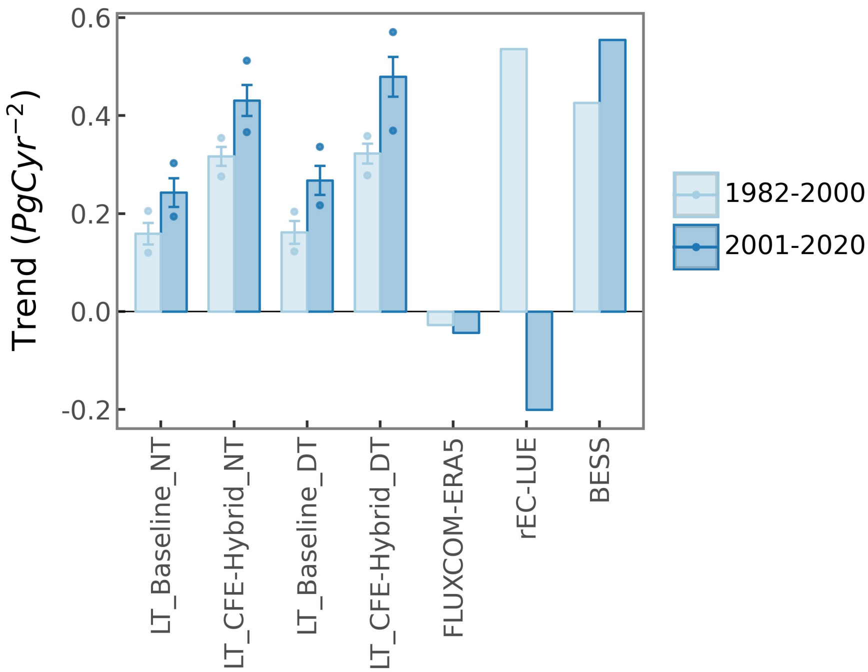

Figure S17. Comparison of global annual GPP trend over 1982-2000 and over 2001-2020 in CEDAR-GPP, FLUXCOM-ERA5, rEC-LUE, and BESS.

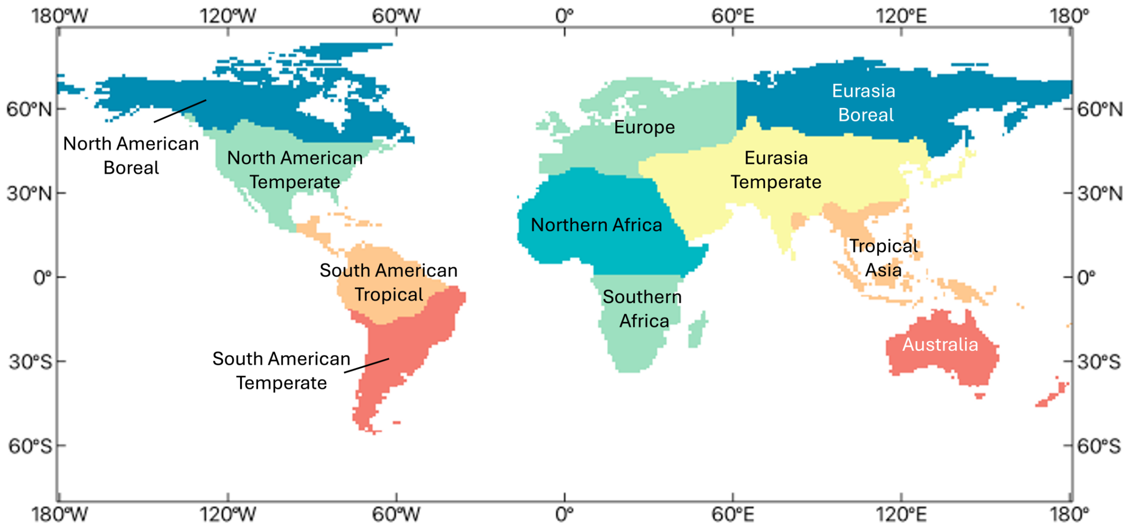

Figure S18. Map of 11 TransCom land regions. The Atmospheric Tracer Transport Model Intercomparison Project (TransCom) was a research initiative for quantifying uncertainties in inversion calculations of the global carbon budget, and the regions were defined to compare and assess carbon budget at regional to global scales (Gurney et al., 2002).

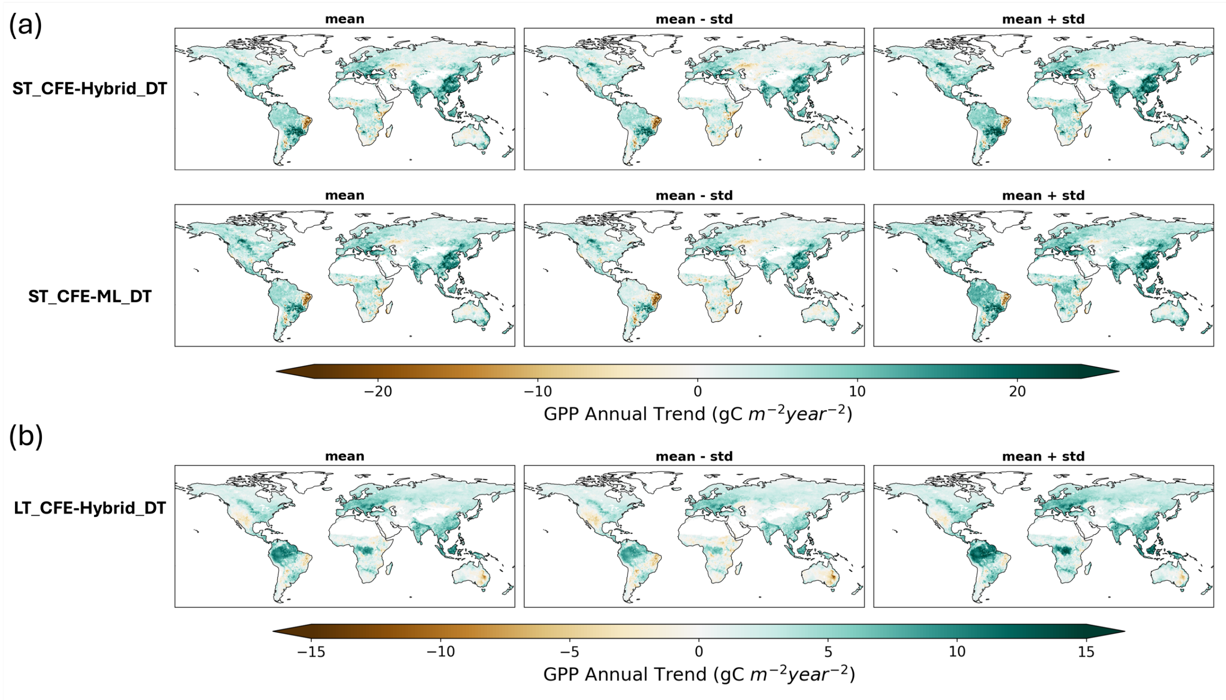

Figure S19. Maps of GPP trends and uncertainty range for CEDAR-GPP CFE datasets (DT only). The first column presents ensemble mean trends, the second column shows trends from the mean minus one standard deviation (upper, and third column indicates the trend from the mean plus one standard deviation. (a) Trends from the short-term (ST) datasets evaluated from 2001 to 2020. (b) Trends from the long-term (LT) dataset evaluated from 1982 to 2020.

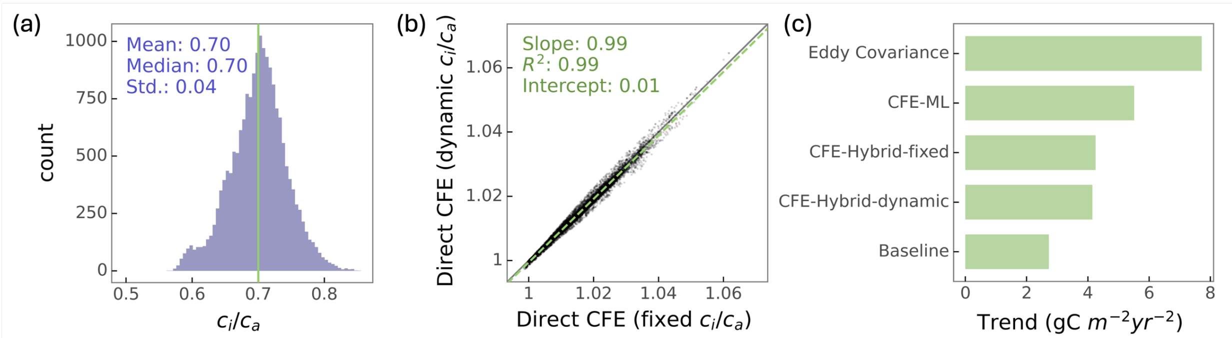

Figure S20. Comparison of CO_2 sensitivity of LUE with dynamic vs. fixed values of χ, i.e. the leaf internal to atmospheric CO_2 concentration ratio (ci/ca). The dynamic model simulates χ as a function of air temperature and VPD, whereas the other approach has a fixed χ at the global long-term average (χ=0.7). (a) Statistical distribution of ci/ca (monthly values) across global eddy covariance towers estimated by the dynamic model. (b) Comparison of the direct CO_2 fertilization effect (CFE) between the two models. The direct CFE is quantified as the ratio between LUE under ambient CO_2 levels and LUE at a reference CO_2 level (the value of year 2001). This ratio corresponds to the ($\phi_{CO_2}^{t}/\phi_{CO_2}^{t_0}$) term in Eq. A8. (c) Aggregated GPP trends across global flux towers over 2002 to 2019 from eddy covariance data and model estimates. The CFE-Hybrid-fixed model assumes a constant ci/ca and the CFE-Hybrid-dynamic model computes ci/ca as a function of air temperature and VPD based on an eco-evolutionary optimality theory.

SI References

Badgley, G., Field, C. B., and Berry, J. A.: Canopy near-infrared reflectance and terrestrial photosynthesis, Science Advances, 3, 1–6, https://doi.org/10.1126/sciadv.1602244, 2017.

Camps-Valls, G., Campos-Taberner, M., Moreno-Martínez, Á., Walther, S., Duveiller, G., Cescatti, A., Mahecha, M. D., Muñoz-Marí, J., García-Haro, F. J., Guanter, L., Jung, M., Gamon, J. A., Reichstein, M., and Running, S. W.: A unified vegetation index for quantifying the terrestrial biosphere, Science Advances, 7, eabc7447, https://doi.org/10.1126/sciadv.abc7447, 2021.

Gao, B. C.: NDWI - A normalized difference water index for remote sensing of vegetation liquid water from space, Remote Sensing of Environment, 58, 257–266, https://doi.org/10.1016/S0034-4257(96)00067-3, 1996.

Gitelson, A. a.: Remote estimation of canopy chlorophyll content in crops, Geophysical Research Letters, 32, L08403, https://doi.org/10.1029/2005GL022688, 2005.

Gurney, K. R., Law, R. M., Denning, A. S., Rayner, P. J., Baker, D., Bousquet, P., Bruhwiler, L., Chen, Y.-H., Ciais, P., Fan, S., Fung, I. Y., Gloor, M., Heimann, M., Higuchi, K., John, J., Maki, T., Maksyutov, S., Masarie, K., Peylin, P., Prather, M., Pak, B. C., Randerson, J., Sarmiento, J., Taguchi, S., Takahashi, T., and Yuen, C.-W.: Towards robust regional estimates of CO2 sources and sinks using atmospheric transport models, Nature, 415, 626–630, https://doi.org/10.1038/415626a, 2002.

Still, C. J., Berry, J. A., Collatz, G. J., and DeFries, R. S.: ISLSCP II C4 Vegetation Percentage, in: Hall, Forrest G., G. Collatz, B. Meeson, S. Los, E. Brown de Colstoun, and D. Landis (eds.). ISLSCP Initiative II Collection. Data set., http://dx.doi.org/10.3334/ORNLDAAC/932, 2009.